

Coronal loop slow mode oscillations driven by the kink instability

M. Haynes, T. D. Arber, and E. Verwichte

Centre for Fusion, Space and Astrophysics, Physics Department, Warwick University, Coventry, CV4 7AL, UK
e-mail: martin.haynes@warwick.ac.uk

Received 23 August 2007 / Accepted 7 December 2007

ABSTRACT

Aims. To establish the dominant wave modes generated by an internal, $m = 1$ kink instability in a short coronal flux tube.

Methods. The 3D MHD numerical simulations are performed using Lare3d to model the kink instability and the subsequent wave generation. The initial conditions are a straight, zero net current flux tube containing a twist higher than the kink instability threshold.

Results. It is shown that the kink instability initially sets up a 1st harmonic (1st overtone) that is converted through the rearrangement of the magnetic field into two out-of-phase fundamental slow modes. These slow modes are in the two entwined flux tubes created during the kink instability.

Conclusions. The long-lived oscillations established after a kink instability provide a possible way to identify whether sudden, short coronal loop brightenings may have resulted from a confined kink instability. The mode oscillation structure changes from the 1st harmonic to fundamental due to field line relaxation. The subsequent decay in the fundamental mode is comparable to observations and is caused by shock dissipation. This result has important consequences for the damping of the slow mode oscillations observed by SUMER.

Key words. Sun: corona – Sun: magnetic fields – Sun: oscillations – Sun: flares

1. Introduction

There is observational evidence of standing slow mode oscillations in the solar corona (Kliem et al. 2002; Wang et al. 2002) and Wang et al. (2003) also investigated a sample of 54 Doppler shift oscillations and concluded that they were standing slow modes. However, the generation of standing slow modes is an area of ongoing research that puts most emphasis on impulsive flare generation. A high proportion of the previous work on slow mode wave generation has been done in 1D loop codes where the simulation domain is assumed to be along the magnetic field line. The wave generation mechanism in these cases is the energy deposited by different flare models. For example, Nakariakov et al. (2004) and Tsiklauri et al. (2004) studied the generation of the slow mode 1st harmonic by loop apex heating. For clarity, the mode naming used throughout this paper is that the 1st harmonic refers to the standing mode with a velocity node at the midpoint, i.e. the 1st overtone. Selwa et al. (2005) investigated the dependence of the generation of the fundamental and the 1st harmonic on the perturbation position within the loop. Taroyan et al. (2005) looked both analytically and numerically at the generation of the fundamental mode due to impulsive foot-point heating. All of these previous works used an arbitrarily imposed driver to generate the modes. However, here the wave modes are established self consistently from the kink instability. From the studies of Nakariakov et al. (2000), Ofman & Wang (2002) and De Moortel & Hood (2003) it was concluded that the dominant mechanism responsible for the damping of slow modes is thermal conduction. The 1D nature of the previous wave generation works allowed the straightforward inclusion of non-ideal thermal transport terms. In this 3D work the only non-ideal thermal term is current triggered, anomalous resistivity leading to localised Ohmic heating.

Previous work on the kink instability has focused on the properties of the kink instability and its evolution in both the context of flares and coronal mass ejections (CMEs). For example there has been much interest on the generation of the currents (Baty & Heyvaerts 1996; Velli et al. 1997; Baty 1997; Lionello et al. 1998; Arber et al. 1999; Baty 2000; Gerrard & Hood 2003) and how they are affected by the twist (Gerrard et al. 2001, 2002). All of this work focused on the short, straight tube approximation. Work has also been done looking at the effects of curvature on the stability of loops (Török & Kliem 2003; Török et al. 2004; Aulanier et al. 2005; Birn et al. 2006) and the subsequent evolution of the field (Amari et al. 1996; Amari & Luciani 1999; Tokman & Bellan 2002; Török & Kliem 2003; Gerrard et al. 2004; Fan 2005; Török & Kliem 2005).

Here we concentrate on the oscillatory mode development after the kink instability has occurred in a short, hot, dense loop. This is achieved by running a simulation equivalent to the one in Arber et al. (1999) and Haynes & Arber (2007) but instead of only running for the dynamic phase the simulation is extended to establish any wave modes set up in the resulting magnetic structure. The kink instability studied is the non-eruptive, confined kink instability in a loop which initially carries no net current.

2. Techniques

The simulations were run using the code Lare3d (Arber et al. 2001) which numerically integrates the resistive MHD equations in normalised, Lagrangian form.

The normalisation used throughout this paper is the same as that of Haynes & Arber (2007) and is summarised below. The defined quantities are

$$L_0 = 1 \text{ Mm}$$

$$B_0 = 2 \times 10^{-3} \text{ T (20 G)}$$

$$\rho_0 = 1.67 \times 10^{-12} \text{ kg m}^{-3}$$

leading to the derived normalising quantities

$$v_A = 1.38 \times 10^6 \text{ m s}^{-1}$$

$$t_0 = 1 \text{ s}$$

$$T_0 = 1 \times 10^8 \text{ K.}$$

In the MHD equations below the velocities are normalised to the Alfvén speed $v_0 = B_0 / \sqrt{\mu_0 \rho_0}$, the current density is normalised to $j_0 = B_0 / (\mu_0 L_0)$, the resistivity to $\eta_0 = (\mu_0 L_0 v_0)^{-1}$ and the pressure to $P_0 = B_0^2 / \mu_0$.

$$\frac{D\rho}{Dt} = -\rho \nabla \cdot \mathbf{v} \quad (1)$$

$$\frac{D\mathbf{v}}{Dt} = \frac{1}{\rho} (\nabla \times \mathbf{B}) \times \mathbf{B} - \frac{1}{\rho} \nabla P \quad (2)$$

$$\frac{D\mathbf{B}}{Dt} = (\mathbf{B} \cdot \nabla) \mathbf{v} - \mathbf{B} (\nabla \cdot \mathbf{v}) - \nabla \times (\eta \nabla \times \mathbf{B}) \quad (3)$$

$$\frac{D\epsilon}{Dt} = -\frac{P}{\rho} \nabla \cdot \mathbf{v} + \frac{\eta}{\rho} j^2. \quad (4)$$

Where D/Dt is the advective derivative, and the normalised current density is defined as $\mathbf{j} = \nabla \times \mathbf{B}$. ϵ is the specific internal energy leading to the equation of state $P = \rho \epsilon (\gamma - 1)$, where $\gamma = 5/3$ is the ratio of specific heats.

The resistivity model used is of the following form

$$\eta = \begin{cases} 0 & , |\mathbf{j}| < 5 \\ 1 \times 10^{-3} & , |\mathbf{j}| \geq 5. \end{cases} \quad (5)$$

This ensures that the resistivity is only applied in regions of large current density leading to a less diffuse solution than would have been obtained using uniform resistivity (Arber et al. 1999).

3. Initial conditions

The initial conditions used in this paper are the same as those in Arber et al. (1999) and Haynes & Arber (2007).

The computational domain has the normalised dimensions $-6 \leq x, y, \leq 6$ and $-5 \leq z \leq 5$. The flux tube is initialised as running along the z axis within a radius of 1 giving a tube length of 10. The z boundary conditions are line-tied and the x, y boundaries are set to zero gradient with a velocity damping region of width 0.6 covering the region just inside the boundary. The results presented here are from a simulation run using $256 \times 256 \times 128$ grid points, the grid is stretched in the x and y directions giving a minimum grid spacing of 0.03 in these directions over the central region $|x, y| < 2$. The z spacing is uniform giving a minimum spacing of 0.08. The results were tested for convergence using a grid of $512 \times 512 \times 256$.

The initial plasma conditions are set to a uniform normalised temperature of 0.01 (1×10^6 K) and a uniform normalised density of 1 (1.67×10^{-12} kg m $^{-3}$).

The initial magnetic field is set to a force-free, kink unstable loop which carries no net current. The field is determined from the condition that the loop carries no net current and that the current is completely contained within $r = 1$

$$\int_0^1 r j_z(r) dr = 0 \quad (6)$$

which for j_z of the form

$$j_z = j_i \left(1 - \frac{r^2}{b^2} + a \frac{r^3}{b^3} \right) \quad (7)$$

is satisfied if $a = 5/6^{3/2}$ and $b = 1/6^{1/2}$. The component B_θ is then found from j_z , which gives the x and y components of \mathbf{B} . Using Ampère's law, B_z is found from the force-free condition

$$B_z^2 = B_i^2 - B_\theta^2 - 2 \int_0^r \left(\frac{B_\theta^2}{r'} \right) dr'. \quad (8)$$

This leaves the values of B_z and j_z on the axis as free parameters; these are chosen as $B_i = 1.0$ and $j_i = 4.3$.

This choice of initial conditions places the average twist in the loop above the kink instability threshold for the Gold-Hoyle equilibrium of $\phi_{\text{crit}} = 2.49\pi$ (Hood & Priest 1981). A small velocity perturbation with the structure found from the linear analysis in Arber et al. (1999) is also applied to the loop to initialise the onset of the instability.

4. Simulation evolution

The simulation was run until $t = 1000$ to allow any wave modes present to establish. For reference the kink instability and associated reconnection is completed by $t = 200$.

Figure 1 shows snapshots from the simulation both during and after the kink instability. The simulation starts with a small velocity perturbations initialising the kink instability. The first two snapshots in Fig. 1 show the initial field configuration and the subsequent onset of the kink instability.

The kink instability drives the axis of the flux tube into a helix, this forces the twisted internal field against the straight outer field. This compression of the field generates a current sheet wrapped around the flux tube. This current sheet can be clearly seen in the $t = 20$ snapshot in Fig. 1. The current sheet magnitudes increases until $|\mathbf{j}| \geq 5$ switching on the resistivity as given in Eq. (5). This switching on of the resistivity marks the end of the linear phase of the kink instability.

The resistivity now present in the current sheet allows reconnection between the twisted internal field and the external field. The newly connected field lines therefore now have a straight section outside the original tube and a twisted section inside the tube. A field line with this configuration can be seen in Fig. 1 at $t = 60$. In front of the tube a straight blue field line can be seen rising from the bottom of the domain then entering the tube through the current sheet and becoming more twisted. Due to the reconnection outflows the velocity along the straight portion of this field line will be towards the bottom boundary, whereas the flow in the twisted region will be towards the top. These flows will tend to drive the 1st harmonic.

Figure 2 shows v_z plotted against z for two different times. The top plot is at $t = 30$, plotted along $(x, y) = (0.875, 0)$ which is the line passing through the strongest current region at this time. The reconnection outflows are shown to be driving the 1st harmonic. The bottom plot is at $t = 200$, plotted along $(x, y) = (0, -0.875)$ and it shows a dominant fundamental. The line chosen for the bottom plot is different to the top due to the line used for the top plot now passing through both the red and blue flux tubes shown in the last snapshot of Fig. 1. The line is therefore moved to a position where it is almost entirely contained in the blue tube. This second position could not be used for the earlier plot due to it passing through multiple reconnection sites and therefore showing predominantly higher harmonics.

For the magnetic field the result of this reconnection is the field lines having an uneven distribution of twist, i.e. the newly reconnected field lines have a straight section external to the tube

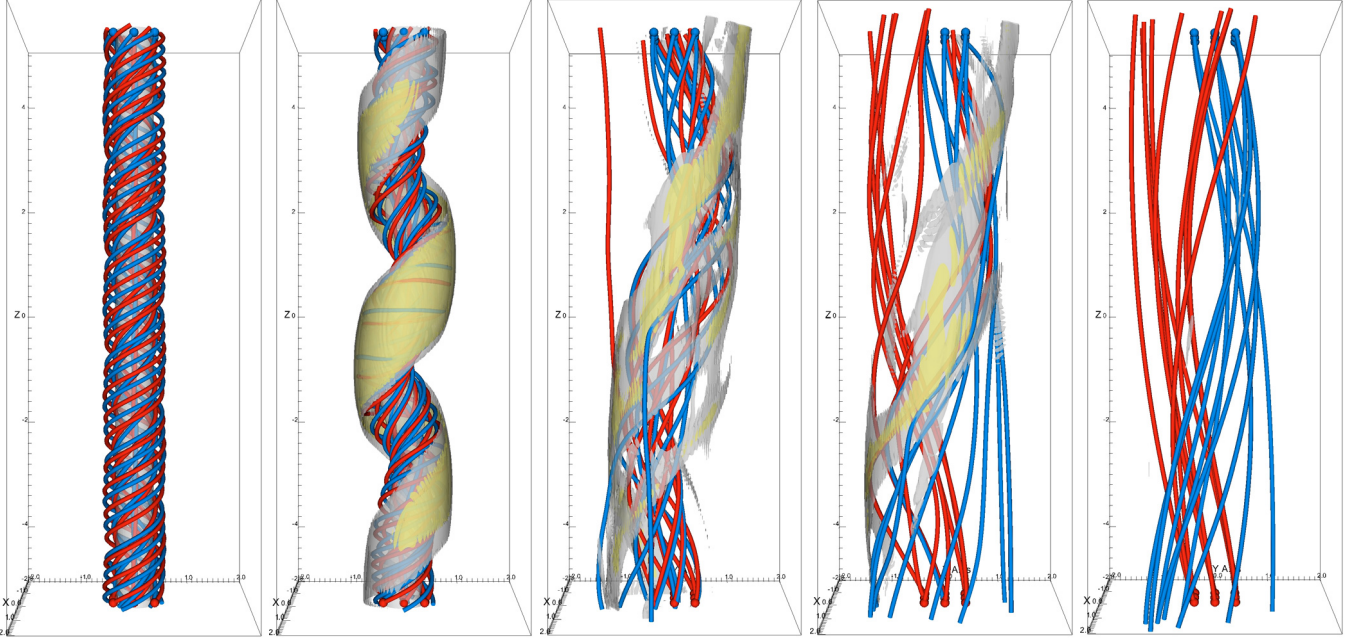


Fig. 1. Snapshots showing the evolution of the central region of the simulation. From *left to right* the snapshots are at $t = 0, 20, 60, 100, 200$. The semi-transparent isosurfaces are where $|J| = 3$, shown in grey, and $|J| = 5$, shown in yellow. The magnetic field lines are traced from the z boundaries starting within a radius of 0.5, the red field lines are traced from the *bottom* boundary and the blue lines from the *top*.

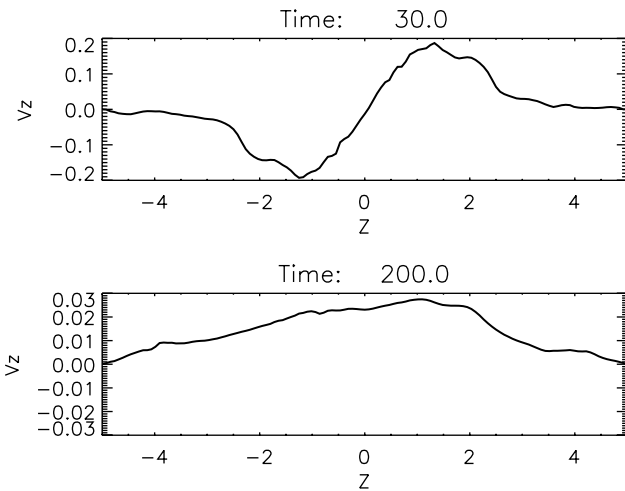


Fig. 2. Plots showing v_z against z . *Top* at $t = 30$ along the line $(x, y) = (0.875, 0)$. *Bottom* at $t = 200$ along the line $(x, y) = (0, -0.875)$.

and a twisted section inside the tube. This configuration will redistribute the twist evenly along the field line. Once all the reconnection has finished and the field lines have relaxed, the final state of the field lines is shown in the $t = 100$ snapshot in Fig. 1. The field now consists of two twisted flux tubes, each one connecting the original ends of the flux tube to the external field region at the opposite boundary. For example the blue flux tube has one end inside the original flux tube at the top boundary but connected to a region outside the flux tube at the bottom boundary. The lower snapshot in Fig. 2 shows the field aligned velocity once the field has settled into this final state. It can be seen that the dominant wave mode is now the fundamental, although there are still some higher harmonics present.

Figure 3 shows the field aligned velocity at the centre of the two new structures as a function of time, showing the presence

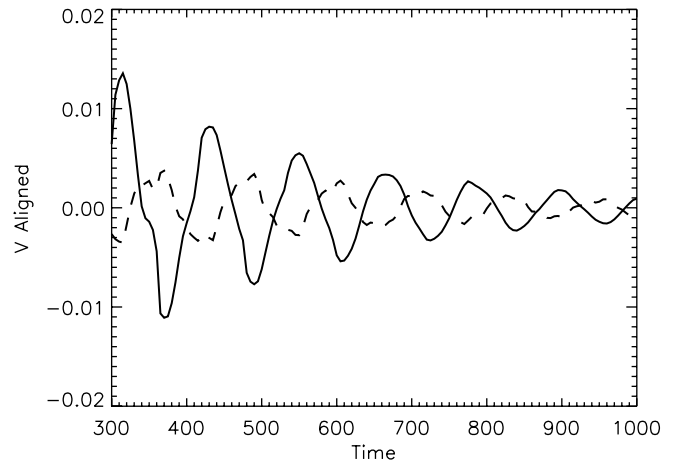


Fig. 3. Plot of the field aligned velocity against time for the two separate loops shown in the final snapshot in Fig. 1. The points used to measure the velocity are $(x, y, z) = (0, \pm 1, 0)$, which were chosen so one point was in the blue flux tube and the other in the red flux tube.

of out-of-phase, oscillating field aligned flows. The amplitude of the waves differs because the position of the points used to measure the velocity are not at the same relative location inside the two final tube structures. The structure of the flow along the field line shown in Fig. 2 at $t = 830$ suggests that these flows are predominantly a fundamental compressible mode. Figure 4 shows the amplitude of the frequency components of the velocity plots in Fig. 3, the vertical dashed line shows the frequency of the fundamental slow mode calculated from the average tube speed in the flux tube. The average tube speed, $\bar{c}_t = c_s v_a / \sqrt{c_s^2 + v_a^2}$, over all z within $r = 2$ is $\bar{c}_t = 0.15 \pm 0.03$. The error is taken to be the standard deviation of the values used to calculate the average. The two tubes are of length $L_z = 10$, this gives a

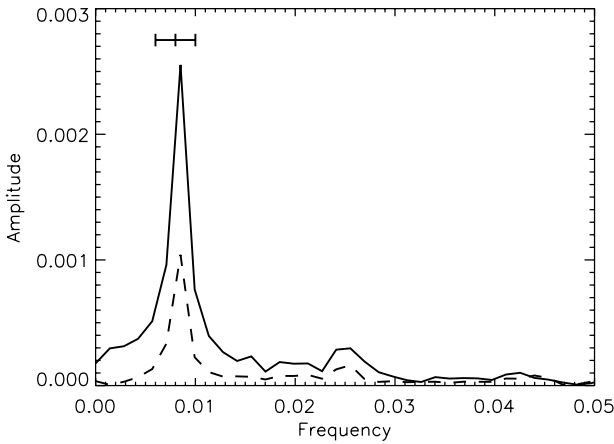


Fig. 4. Plot of the amplitude of the Fourier components of the oscillations plotted in Fig. 3 with the same line styles as in Fig. 3. The Fourier transform was taken over the time domain $300 \leq t \leq 1000$ without windowing. The error bar shows the frequency, and associated error, of the fundamental slow mode predicted from the average tube speed.

fundamental frequency of 0.008 ± 0.002 , or an oscillation period of 130 ± 25 . The Fourier spectra of the two oscillations both show strong peaks at the frequency corresponding to the fundamental slow mode. For comparison the fundamental frequency calculated from the average and standard deviation of the Alfvén speed is 0.023 ± 0.002 .

5. Discussion

The results presented here raise a couple of interesting questions: how does the 1st harmonic evolve into the fundamental and what is damping the fundamental slow mode?

The proposed mechanism for the conversion of the 1st harmonic into the fundamental is tied in with the post reconnection field lines. The region with the strongest reconnection is half way along the loop where the current sheet magnitude is highest. The reconnection drives flows away from this point along the newly reconnected field lines. As this driving point is predominantly close to the centre of the flux tube it drives a 1st harmonic in both flux tubes as a function of the z coordinate. While in the z direction the velocity node is in the centre of the tube, and hence appears as the 1st harmonic, this is not true along the fieldline coordinate. The field line is composed of a straight section, external to the original tube, and a twisted internal section. Therefore the node in velocity along the fieldline is actually closer to the end of the flux tube to which it is connected by the shorter, straight section of the fieldline. The field line relaxes to a final state in which the twist is uniformly distributed. In this process the velocity node in z moves towards the boundary connected to the originally straight field line section. When analysed as Fourier modes in z this appears to be a decay of the 1st harmonic and a growth of the fundamental mode. Figure 5 shows the amplitude of the fundamental and 1st harmonic Fourier components, obtained from the spatial Fourier transform of v_z along the line $(x, y) = (0, -0.875)$ which is the same line used in the bottom plot of Fig. 2. In Fig. 5 the black line shows the amplitude of the fundamental component and the dotted line shows the amplitude of the 1st harmonic. It can be seen that initially the 1st harmonic is generated, however this then decays rapidly leaving the dominant fundamental component. The 1st harmonic decays

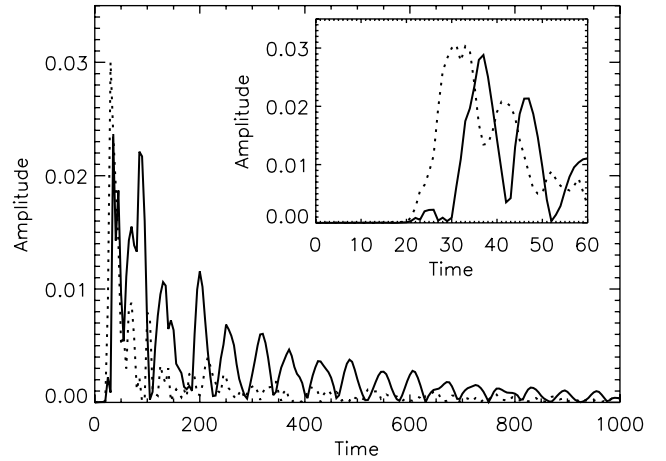


Fig. 5. Plot showing the time evolution of the amplitude of the fundamental and 1st harmonic Fourier components of v_z , using a spatial Fourier transform along the line $(x, y) = (0, -0.875)$. The solid line shows the fundamental component amplitude and the dotted line shows the 1st harmonic. The inset plot shows the period from $0 \leq t \leq 60$ to clarify the initial growth.

on a similar time scale to the field relaxation, i.e. the Alfvén transit time along $L_z/2$, which is approximately 5 in normalised units. This provides circumstantial evidence for the decay being caused by the straightening of the field lines.

It must be stressed however that this is a purely geometric effect and to leading order the mode structure along a field line coordinate doesn't change. Because it is the twisted internal section of the loop which expands to produce the fundamental it is the phase of this half of the 1st harmonic which sets the phase of the fundamental. The out flows from the reconnection region are symmetric about the centre thus the opposite ends of the field lines have opposite sign in velocity. As the central nodes in the two flux tubes expand towards different ends this opposite sign leads to the observed out phase behaviour of the fundamental modes.

The damping of the fundamental seen in Figs. 3 and 5 can be explained through shock damping. From Fig. 3, the slow modes have an initial amplitude of $a \sim 0.02v_A$. In terms of the local sound speed (c_s) this gives an oscillation amplitude of $a \sim 0.12c_s$. The wave number of the fundamental mode is $k = 2\pi/20$. For harmonic slow waves the time to shock formation is given by $t_s = c_s/ak$ so that the fundamental modes will form shocks at $t \sim 26$. Figure 3 shows the amplitude evolution over a timescale ~ 700 so that the slow modes will shock early in this interval. Shock viscosity (see Arber et al. 2001) for simple compressive sound waves is applied by adding scalar viscosity (q) to the pressure of the form $q = \nu c_s \Delta x |\nabla \cdot v|$, where Δx is the computational cell size and $\nu = 0.05$, whenever $\nabla \cdot v < 0$. As the resolution is increased this tends to zero for smooth solutions and to a constant value of $q = \nu c_s \Delta v$, where Δv is the jump in velocity across the shock, at shock fronts. Thus for resolved solutions doubling the resolution will not change this shock viscosity but it will reduce numerical viscosity. This has been confirmed by higher resolution convergence tests which give the same decay rate as reported above. The choice of ν is from experiments at lower resolution and standard shock tests and ensures there are no false oscillations generated at shocks. The dissipation due to shock formation is therefore a real physical process and not the result of numerical dissipation.

To investigate other possible contributions to the damping of the fundamental modes the outward Poynting flux through a closed domain surrounding the two entwined flux tubes was also monitored. Poynting's theorem was satisfied to 0.001% accuracy in the code. For the simulations presented above there is significant wave activity resulting from the fast waves driven by the initial kink instability. This dominates the outward fluxes and is larger than the energy loss from the slow modes. The presence of fast waves driven by the instability make it difficult to determine if the slow mode is decaying due to a coupling to radiating fast modes. To clarify, the code was run for longer, i.e. until $t = 3000$ at which time all oscillations had decayed to a level below that of the fundamental mode observed at $t = 400$. The code was then restarted from this relaxed state but with the parallel velocity from $t = 400$ added back. This then gave a clean start to the fundamental modes with no oscillations left from the kink instability. This fundamental decayed at the same rate as depicted in Fig. 3 and this time there was no evidence of a net outward Poynting flux comparable to the energy loss from the fundamental modes. For this simulation the total shock viscous heating was also monitored and this matched the energy loss from the fundamental slow mode oscillations. It is therefore concluded that the damping of the fundamental slow modes is due to shock dissipation with no significant contribution from mode coupling to a radiating fast wave.

6. Conclusion

Numerical experiments were run to ascertain the waves generated following the confined, $m = 1$ internal kink instability in a short, hot coronal loop. These experiments have shown that initially 1st harmonic (1st overtone) slow mode are observed in the two post-reconnection flux tubes. The velocity node is at the mid-point of each flux tube. However, this does not match the mid-point of the magnetic field line because of the magnetic twist. As the twist along the fieldline becomes uniform the velocity node moves to one of the footpoints, which is observed as the damping of the 1st harmonic and the appearance of the fundamental mode. This is purely due to the geometry of the evolving field structure and does not actually involve a damping or excitation mechanism once the field aligned reconnection driven flow is initiated. The period of the fundamentals generated is 125 ± 25 s in a loop 10 Mm long. These two entwined, out-of-phase, fundamental slow mode loops would provide a diagnostic for post kink loops in the corona. Using this diagnostic should therefore aid in the identification of post-kink loops once the modes present have been established.

As can be seen from Fig. 3 once the oscillatory phase is established the waves damp quickly. This damping rate is similar to that seen from the inclusion of non-ideal terms (e.g. Nakariakov et al. 2000; Ofman & Wang 2002; De Moortel & Hood 2003). However, this damping is not due to the resistivity as the currents present during this stage of the simulation remain below the value required to trigger the resistivity. Likewise thermal conduction, which has been shown to efficiently damp slow modes, is not included. The damping has been shown to be due to shock dissipation with no significant contribution from mode coupling to a radiating fast wave. Shock dissipation is of particular relevance to the observed slow mode oscillations in coronal loops by SUMER. Of the slow mode oscillations reported by Wang et al. (2003) 74% have Mach numbers above 0.1 and 43% have Mach numbers above 0.2. Hence, nonlinear effects can be important. From shock dissipation in 1D acoustics, the oscillation is expected to damp over a time-scale proportional to the

wavelength and inversely proportional to the velocity amplitude. Although future work is needed to accurately characterise the shock behaviour of slow magnetoacoustic modes in structured coronal loops, it is possible to give some estimates of what the damping time may be for the range of loop lengths and velocity amplitudes observed by SUMER. The simulations show for a slow mode with wavelength $\lambda_0 = 20$ Mm and velocity amplitude $a = 0.12 C_s$ an e-folding damping time of $\tau_0 \approx 150\text{--}200$ s. An estimate for the damping time for arbitrary wavelength and velocity amplitude is $\tau = \tau_0(\lambda/\lambda_0)(a/a_0)^{-1}$. For $\lambda = 200$ Mm and $a \sim 0.2C_s$, we find $\tau = 15\text{--}20$ min. This time is comparable to the observed damping times as well as to the thermal conduction time-scale. Therefore, we conclude that the effect of shock dissipation on the damping of SUMER slow mode oscillations may be important, especially for shorter loops, and warrants further investigation (e.g. parameter studies of shocking slow modes with varying loop lengths and velocity amplitudes).

The out-of-phase fundamental slow modes would provide a useful diagnostic when looking for evidence of the kink instability occurring in short, hot loops. This current work uses a straight tube approximation therefore further work is under way to establish whether these results are still present when curved geometry is used.

Acknowledgements. This work was sponsored in part by the United Kingdom Particle Physics and Astronomy Research Council. The computational work was supported by resources made available through the UK MHD Consortium and Warwick University's Centre for Scientific Computing.

References

- Amari, T., & Luciani, J. F. 1999, *ApJ*, 515, L81
- Amari, T., Luciani, J. F., Aly, J. J., & Tagger, M. 1996, *ApJ*, 466, L39
- Arber, T. D., Longbottom, A. W., & Van der Linden, R. A. M. 1999, *ApJ*, 517, 990
- Arber, T. D., Longbottom, A. W., Gerrard, C. L., & Milne, A. M. 2001, *J. Comput. Phys.*, 171, 151
- Aulanier, G., Démoulin, P., & Grappin, R. 2005, *A&A*, 430, 1067
- Baty, H. 1997, *A&A*, 318, 621
- Baty, H. 2000, *A&A*, 360, 345
- Baty, H., & Heyvaerts, J. 1996, *A&A*, 308, 935
- Birn, J., Forbes, T. G., & Hesse, M. 2006, *ApJ*, 645, 732
- De Moortel, I., & Hood, A. W. 2003, *A&A*, 408, 755
- Fan, Y. 2005, *ApJ*, 630, 543
- Gerrard, C. L., & Hood, A. W. 2003, *Sol. Phys.*, 214, 151
- Gerrard, C. L., Arber, T. D., Hood, A. W., & Van der Linden, R. A. M. 2001, *A&A*, 373, 1089
- Gerrard, C. L., Arber, T. D., & Hood, A. W. 2002, *A&A*, 387, 687
- Gerrard, C. L., Hood, A. W., & Brown, D. S. 2004, *Sol. Phys.*, 222, 79
- Haynes, M., & Arber, T. D. 2007, *A&A*, 467, 327
- Hood, A. W., & Priest, E. R. 1981, *Geophysical and Astrophysical Fluid Dynamics*, 17, 297
- Kliem, B., Dammasch, I. E., Curdt, W., & Wilhelm, K. 2002, *ApJ*, 568, L61
- Lionello, R., Velli, M., Einaudi, G., & Mikić, Z. 1998, *ApJ*, 494, 840
- Nakariakov, V. M., Verwichte, E., Berghmans, D., & Robbrecht, E. 2000, *A&A*, 362, 1151
- Nakariakov, V. M., Tsiklauri, D., Kelly, A., Arber, T. D., & Aschwanden, M. J. 2004, *A&A*, 414, L25
- Ofman, L., & Wang, T. 2002, *ApJ*, 580, L85
- Selwa, M., Murawski, K., & Solanki, S. K. 2005, *A&A*, 436, 701
- Taroyan, Y., Erdélyi, R., Doyle, J. G., & Bradshaw, S. J. 2005, *A&A*, 438, 713
- Tokman, M., & Bellan, P. M. 2002, *ApJ*, 567, 1202
- Török, T., & Kliem, B. 2003, *A&A*, 406, 1043
- Török, T., & Kliem, B. 2005, *ApJ*, 630, L97
- Török, T., Kliem, B., & Titov, V. S. 2004, *A&A*, 413, L27
- Tsiklauri, D., Nakariakov, V. M., Arber, T. D., & Aschwanden, M. J. 2004, *A&A*, 422, 351
- Velli, M., Lionello, R., & Einaudi, G. 1997, *Sol. Phys.*, 172, 257
- Wang, T., Solanki, S. K., Curdt, W., Innes, D. E., & Dammasch, I. E. 2002, *ApJ*, 574, L101
- Wang, T. J., Solanki, S. K., Curdt, W., et al. 2003, *A&A*, 406, 1105